Chapter 6

Impact of Electrode Roughness on Metal-Insulator-Metal (MIM) Diodes and Step Tunneling in Nanolaminate Tunnel Barrier Metal-Insulator-Insulator-Metal (MIIM) Diodes

John F. Conley Jr. and Nasir Alimardani

Abstract In this chapter, the impact of electrode roughness and bilayer insulator tunnel barriers on the performance of metal-insulator-metal (MIM) diodes are discussed. The effect of bottom electrode roughness on the current versus voltage (*I–V*) characteristics of asymmetric electrode M_1IM_2 tunnel diodes is discussed first. Atomic layer deposition (ALD) is used to deposit high quality insulators independent of bottom metal electrode. It is shown that bottom electrode roughness can strongly influence the *I–V* characteristics of M_1IM_2 diodes, overwhelming even the metal work function difference induced asymmetry. Devices with smoother bottom electrodes are shown to produce *I–V* behavior with better agreement with Fowler–Nordheim tunneling theory as well as yield a higher percentage of well-functioning devices. By combining high quality uniform tunnel barriers deposited by ALD with atomically smooth (~0.3 nm RMS roughness) bottom electrodes, highly nonlinear and asymmetric MIM tunnel diodes with good reproducibility and stable *I–V* behavior are produced. Next, the impact of nanolaminate bilayer insulator tunnel barriers on asymmetric metal work function metal-insulator-insulator-metal ($M_1I_1I_2M_2$ & $M_1I_2I_1M_2$) devices is discussed. It is demonstrated that bilayer tunnel barriers can be arranged to either enhance, oppose, or even reverse the asymmetry induced by the asymmetric work function electrodes. These results represent experimental demonstration that step tunneling (a step change in the tunneling distance through a bilayer tunnel barrier) can dominate the *I–V* asymmetry of M_1IIM_2 diodes with asymmetric work function electrodes. By combining bilayer tunnel barriers with asymmetric metal electrodes, devices are made with voltage asymmetry and nonlinearity that exceed that of standard single layer asymmetric electrode M_1IM_2 devices as well as that of symmetric electrode $M_1I_1I_2M_1$ devices.

J.F. Conley Jr., (✉) • N. Alimardani
School of Electrical Engineering and Computer Science,
Oregon State University,
Corvallis, OR 97331, USA
e-mail: jconley@eecs.oregonstate.edu

G. Moddel and S. Grover (eds.), *Rectenna Solar Cells*,
DOI 10.1007/978-1-4614-3716-1_6, © Springer Science+Business Media New York 2013

6.1 Introduction/Background

Thin film MIM-based tunneling devices are seeing renewed interest for high speed applications [1–11]. Besides rectenna solar cells [12–15], as discussed in Chap. 5, these applications include hot electron transistors [16–18], and infrared (IR) detectors [19–24]. MIM diodes have also been proposed for macroelectronics applications [25] such as backplanes for liquid-crystal displays (LCDs) [26]. Before any of these applications can be realized, a manufacturable process will be required that can produce uniform, high quality MIM tunnel devices with high asymmetry and nonlinearity. Despite investigation by many groups over many decades [27–34], progress toward commercialization of MIM-based electronics has been hindered by a lack of a manufacturable process. In particular, inattention to electrode roughness along with the lack of a high quality deposited oxide appears to have slowed development of this technology—most experimental work to date on thin film MIM diodes has focused on the use of thin native dielectrics produced by oxidation or nitridation of an underlying rough polycrystalline metal electrode [3, 4, 7–9, 19–24, 27–34]. The operation of MIM diodes is based on quantum mechanical tunneling through a thin insulating film positioned between two metal electrodes [35, 36]. The impact of roughness can be appreciated if it is remembered that the tunneling probability depends exponentially on the electric field in the thin dielectric film [37, 38]. The tunneling current in a MIM tunnel diode should therefore depend strongly on the atomic scale roughness and the uniformity of the electrode–insulator interfaces [39]. Basic studies on electrode and interface roughness and their correlation with the tunneling current will therefore be very important for the advancement of MIM technology. In Sect. 6.3, the performance of MIM tunnel diodes formed on bottom electrode materials with various levels of RMS roughness is compared. Whereas previous MIM diode work has focused primarily on native oxides, the use of atomic layer deposition (ALD) in this work allows for deposition of the same high quality insulator, independent of the bottom metal electrode. It is shown here that bottom electrode roughness can have a dominant impact on the electrical characteristics of MIM diodes, overwhelming the trends expected based on metal electrode work function differences. It is also shown that as electrode roughness decreases, the percentage yield of well-functioning devices trends higher.

As discussed in Chap. 1, for rectenna-based solar cells as well as other potential applications of MIM diodes, highly asymmetric and nonlinear current vs. voltage (*I–V*) behavior at low applied voltages is desired. The standard approach to achieving asymmetric *I–V* characteristics in tunnel devices is the M_1IM_2 diode—the use of metal electrodes with different work functions ($\Phi_{M1} \neq \Phi_{M2}$) to produce a built-in voltage, $V_{bi} = (\Phi_{M1} - \Phi_{M2})/e$ (where e is the electronic charge) across the tunnel barrier [38, 40]. However, even with low roughness electrodes, the amount of asymmetry achievable using this approach is limited by the V_{bi} ($\Delta\Phi_M$) that can be obtained using practical electrodes. An alternative approach to achieving asymmetric and nonlinear operation is therefore needed. The approach

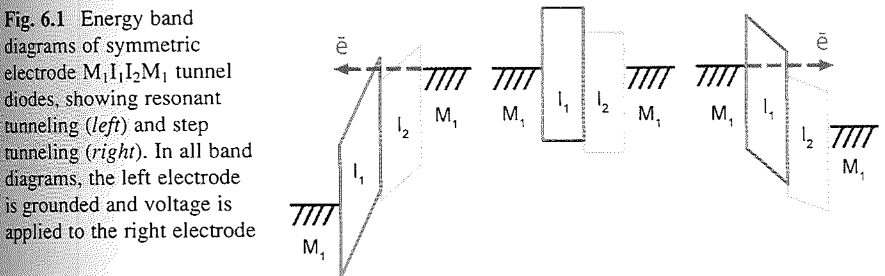

Fig. 6.1 Energy band diagrams of symmetric electrode $M_1I_1I_2M_1$ tunnel diodes, showing resonant tunneling (*left*) and step tunneling (*right*). In all band diagrams, the left electrode is grounded and voltage is applied to the right electrode

investigated in Sect. 6.4 involves engineering of the tunnel barrier so that electrons tunneling from one metal electrode to the other are presented with a different barrier shape depending on the direction of tunneling. Theoretically, formation of an asymmetric tunnel barrier can be accomplished using stacking of insulators [41], with each insulator having different band-gaps (E_G) and electron affinities (χ), to produce metal-insulator-insulator-metal (MI_1I_2M) devices [42, 43].

In Sect. 6.4 the *combined* effect of bilayer tunnel barriers and asymmetric ($\Phi_{M1} \neq \Phi_{M2}$) electrodes are investigated [11]. $M_1I_1I_2M_2$ diodes are fabricated using nanolaminate dielectric bilayers deposited via ALD on smooth bottom electrodes [1, 2]. As illustrated in Fig. 6.1, for a pair of insulators, asymmetry may be enhanced through either resonant tunneling or step tunneling. Whereas most work in the literature has been concerned with resonant tunneling [9, 42, 43], here it is experimentally demonstrated that bilayer insulator tunnel barriers enable tuning of asymmetry (η_{asym}) and nonlinearity (f_{NL}) via step tunneling—the step reduction in the minimum tunnel distance that occurs at the applied bias at which tunneling may begin to take place through only the wider band-gap insulator layer. Experimentally obtained η_{asym} and f_{NL} values are shown to be sensitive to the arrangement of the individual dielectric layers with respect to the larger and smaller Φ_M electrodes (e.g., $M_1I_1I_2M_2$ vs. $M_1I_2I_1M_2$) and it is experimentally demonstrated that bilayer tunnel dielectrics can be arranged to either enhance or oppose (even reverse) the built-in asymmetry of the asymmetric work function electrodes. Finally, it is shown that $M_1I_1I_2M_2$ diodes with superior *I–V* asymmetry can be produced by combining bilayer dielectric tunnel barriers with asymmetric work function metal electrodes.

6.2 Experimental

MIM and MIIM diodes were fabricated on Si substrates capped with 100 nm of thermally grown SiO_2. A typical schematic device cross section is shown in Fig. 6.2. To serve as bottom electrodes, blanket films of either Al, Pt, Ir, or ZrCuAlNi were deposited directly on SiO_2. A thin Ti adhesion layer was used for Pt and Ir. Al was deposited via thermal evaporation, Ir was deposited via

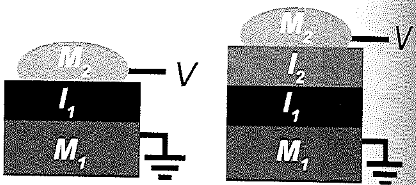

ig. 6.2 Generic schematic ross sections of MIM and IIIM devices used in this tudy

lectron-beam evaporation, and Pt was deposited using either DC sputtering (Pt-1) r electron-beam evaporation (Pt-2). ZrCuAlNi (150 nm thick) was deposited via C magnetron sputtering with no intentional substrate heating using a 3-in. iameter, 0.25-in. thick vacuum arc-melted metal target (with an atomic omposition $Zr_{40}Cu_{35}Al_{15}Ni_{10}$) [2].

Next, thin oxide tunnel barriers (Al_2O_3, HfO_2, and ZrO_2) were deposited via LD using a Picosun SUNALE R-150B ALD reactor. Trimethylaluminum (TMA), trakis (ethylmethylamino) hafnium (TDMAHf), and tetrakis (ethylmethylamino) rconium (TEMAZr) were used as the metal precursors for Al_2O_3, HfO_2, and ZrO_2 espectively. In all cases, deionized water was used as the oxidant. Unless specified, LD films were deposited at a chamber temperature of 250 °C. Nanolaminate ilayer insulators were deposited in one continuous run without breaking vacuum.

Top electrodes were formed by evaporating Al dots (~0.8 mm^2) through a adow mask. I–V analysis was conducted at room temperature on a probe station a dark box using an Agilent 4156C semiconductor parameter analyzer. The noise oor of the measurement system was estimated to be on the order of 10^2 pA. As own in Fig. 6.2, the bottom electrode (M_1) was always held at ground with bias plied to the Al top gate (M_2). To mitigate the impact of displacement current, all V curves were swept from zero bias to either the maximum positive or negative as. Asymmetry, η_{asym}, is defined as negative current divided by positive current | $/I_+|$ so that $\eta_{asym} = 1$ indicates symmetric operation. Non-linearity, f_{NL}, another y figure of merit, is defined as $(dI/dV)/(I/V)$.

Band diagrams were simulated using the Boise State University Band Diagram ogram [44]. Materials parameters used in simulations are consistent with values ported in the literature for similar ALD films: electron affinity (χ) = 1.3 eV, $_G = 6.4$ eV and relative dielectric constant (κ) = 7.6 for Al_2O_3; $\chi = 2.5$ eV, $_G = 5.8$ eV and $\kappa = 18$ for HfO_2; and $\chi = 2.75$ eV, $E_G = 5.4$ eV and $\kappa = 22$ r ZrO_2. Metal work functions (Φ_M) were measured in air using a KP Technology P5050 scanning Kelvin probe over an area of approximately 1 × 1 mm with a 2- m tip and calibrated against a gold standard. The work function of ZrCuAlNi was easured to be approximately 4.8 eV. The relative work function difference tween the ZrCuAlNi and Al electrodes, $\Delta\Phi$ ($=\Phi_{ZrCuAlNi} - \Phi_{Al}$), was easured to be approximately 0.6 eV and was confirmed via extraction from the pe of Fowler–Nordheim (FN) plots. The bottom electrode roughness (RMS and ak) was measured via atomic force microscopy (AFM) using a Digital truments 3 instrument with silicon-nitride tips. Dielectric thickness on Si was easured with a J.A. Woollam WVASE32 spectroscopic ellipsometer using a Cauchy model or via transmission electron microscopy (TEM). TEM images were taken on a FEI Titan 80–200 using samples prepared with a Quanta 3D Dual Beam focused ion beam.

6.3 The Impact of Bottom Electrode Roughness on MIM Devices

In this section, the performance of MIM tunnel diodes formed using ALD deposited Al_2O_3 on low work function (ZrCuAlNi and Al) and high work function (Ir and two types of Pt) bottom electrodes with various levels of RMS roughness is compared.

AFM images of the as-deposited ZrCuAlNi, Pt-1, Pt-2, and Ir bottom electrodes are shown in Fig. 6.3. In order to assess potential roughening as a result of the ALD thermal cycle or interaction of the TMA precursor with the electrodes, additional AFM images were also taken after deposition of a 10 nm Al_2O_3 layer (post-ALD). AFM images of the Al electrode, as-deposited and post-ALD, are shown in Fig. 6.4. (Post-ALD AFM images of the other electrodes are not shown as they show similar properties to the as-deposited films.) As summarized in Table 6.1, the AFM images revealed a wide variation in both RMS average roughness and peak roughness, where roughness values were averaged from a minimum of three images each. With the exception of Pt-2, the RMS and peak roughness tend to scale together. ZrCuAlNi is seen to show the lowest roughness by a factor of 10X. ZrCuAlNi is a well-known

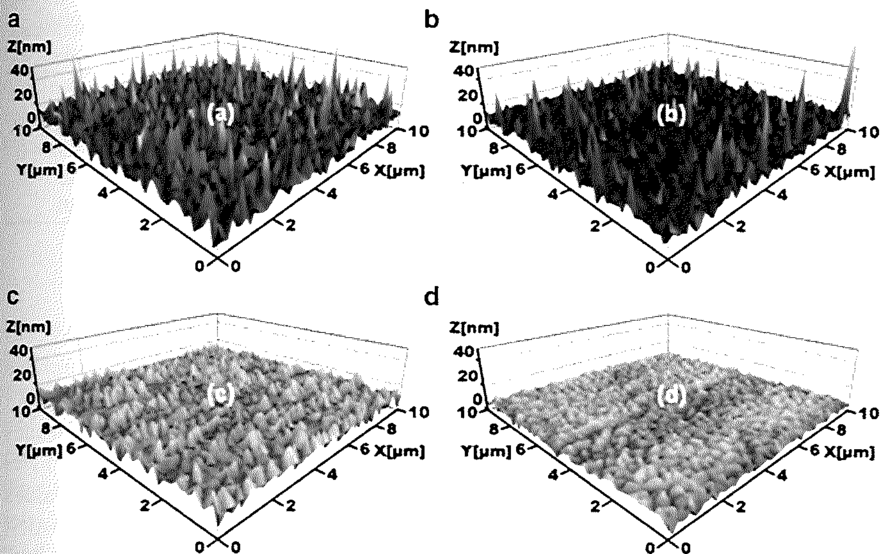

Fig. 6.3 Atomic force microscopy (AFM) images of as-deposited (**a**) Ir, (**b**) electron-beam deposited Pt-2, (**c**) sputtered Pt-1, (**d**) ZrCuAlNi blanket bottom electrodes. Adapted from [1]

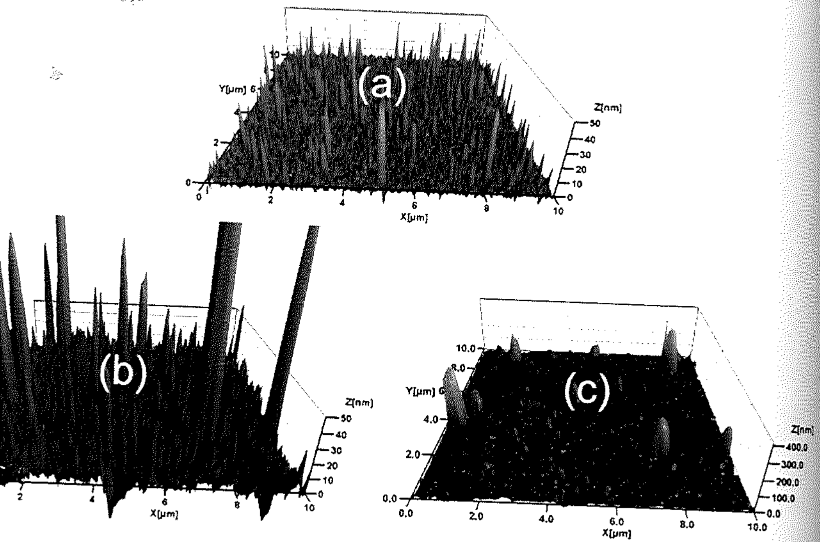

AFM images of the Al electrode (**a**) as-deposited and (**b**, **c**) post atomic layer deposition The post-ALD image is shown on a lower magnification z-scale in (**c**)

.1 Work function, as-deposited and post-ALD RMS and peak roughness, and percentage -functioning devices of metal bottom electrode/10 nm Al_2O_3/Al top electrode M_1IM_2 iodes

e	Φ_M (eV)	Roughness (nm) As-deposited RMS	Peak	Post-ALD RMS	Peak	Functioning devices (%)
	4.2	4	43	21	468	0
eam)	5.3	6 ± 1	220 ± 5	5 ± 1	210 ± 10	<10
	5.1	11 ± 1	120 ± 10	5 ± 1	130 ± 10	30–40
ttered)	5.3	2 ± 0.5	22 ± 5	2 ± 0.5	22 ± 10	30–50
i	4.8	0.3 ± 0.1	3 ± 1	0.3 ± 0.1	3 ± 1	65–80

from [1]

orphous metal [45], and has been used in thin film form for MEMS ons [46, 47]. The very low atomic scale roughness of thin film amorphous expected due to a lack of crystallites and grain boundaries [2, 48]. wing ALD Al_2O_3, some smoothing of the roughest as-deposited electrodes erved. The RMS roughness was improved significantly for Ir (from 11 to nd slightly for Pt-2 (from 6 to 5 nm). On the other hand, roughness values hange significantly for the smoothest as-deposited electrodes, ZrCuAlNi In contrast, as shown in Fig. 6.4, the Al electrodes were found to roughen ximately a factor of 5 after the Al_2O_3 deposition. This increase in s is a consequence of the low melting point of Al and associated grain

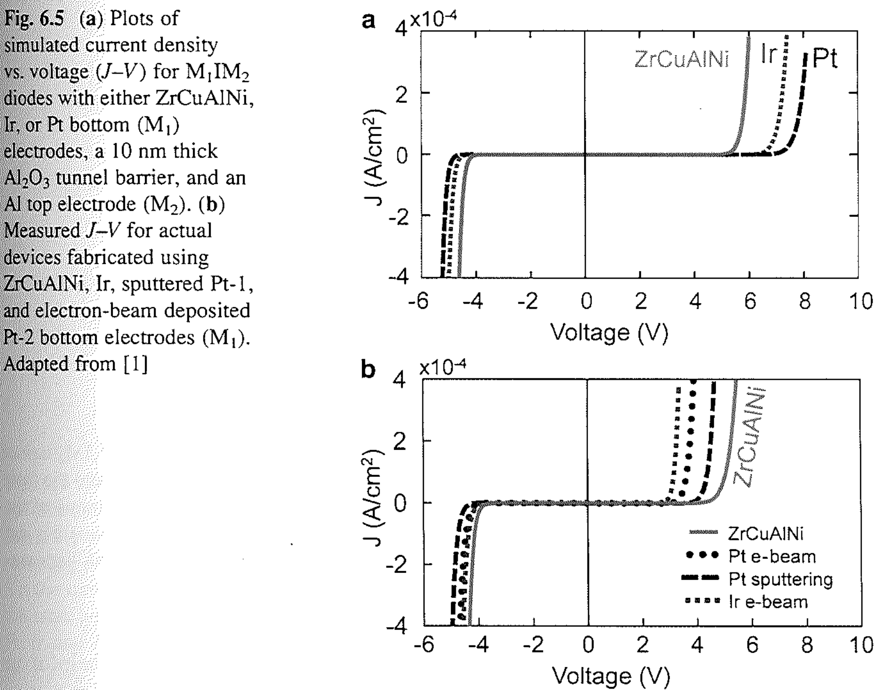

Fig. 6.5 (**a**) Plots of simulated current density vs. voltage (J–V) for M_1IM_2 diodes with either ZrCuAlNi, Ir, or Pt bottom (M_1) electrodes, a 10 nm thick Al_2O_3 tunnel barrier, and an Al top electrode (M_2). (**b**) Measured J–V for actual devices fabricated using ZrCuAlNi, Ir, sputtered Pt-1, and electron-beam deposited Pt-2 bottom electrodes (M_1). Adapted from [1]

growth during the ALD thermal cycle, rather than due to the ALD Al_2O_3 deposition itself.

Shown in Fig. 6.5a, b, are simulated and representative measured J–V curves, respectively, for M_1IM_2 devices with either Ir, Pt, or ZrCuAlNi as the bottom electrodes (M_1), an approximately 10 nm thick Al_2O_3 tunnel barrier, and an Al top electrode (M_2). Simulations are conducted in Matlab using the Fowler–Nordheim (FN) tunneling equation of Simmons [37, 38],

$$J = \frac{q^3}{16\pi\hbar}\left(\frac{m_0}{m_{ox}^*}\right)\frac{1}{\varphi_b}\left(\frac{V+\Delta\varphi}{S}\right)^2 \exp\left(-\frac{4\sqrt{2m_{ox}^*}}{3q\hbar}\frac{S}{V+\Delta\varphi}\varphi_b^{\frac{3}{2}}\right) \quad (6.1)$$

where q is the electron charge, $\hbar$ is the reduced Plank's constant, V is the applied bias, φ_b is the barrier height of the electrode-insulator interface from which electrons are tunneling, $\Delta\varphi$ is the difference in barrier heights between the top and bottom electrode/insulator interfaces (for single insulator layer MIM devices $\Delta\varphi = \Delta\Phi$), m_{ox}^* is the electron effective tunneling mass in the dielectric, and S is the tunnel barrier thickness. It was assumed that the thickness of the Al_2O_3 layer was 10 nm and that the electron effective mass was 0.79 m_0 where m_0 is the mass of the free electron [2, 9]. The only difference between the three simulated curves is the value used for work function of the bottom electrode (Φ_{M1}) as given in Table 6.1 [49], and thus the barrier height of the bottom electrode, $\varphi_{b1}(=\Phi_{M1} - \chi_{Al_2O_3})$.

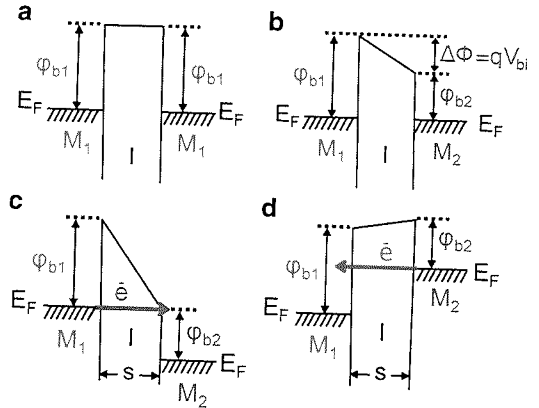

Fig. 6.6 Equilibrium band diagrams of (**a**) symmetric M_1IM_1 and (**b**) asymmetric M_1IM_2 tunnel diodes. φ_{b1} and φ_{b2} indicate the barrier height of the *bottom* (high work function M_1) and *top* (low work function M_2) metal electrodes, respectively. Also shown are energy band diagrams of the asymmetric tunnel diode under (**c**) positive applied bias showing the onset of FN tunneling and (**d**) an equivalent magnitude negative applied bias showing direct tunneling. In all band diagrams, M_1 is grounded and the voltage is applied to M_2

In order to explain the trends in the *J–V* curves in Fig. 6.5, it is helpful to consider MIM energy band diagrams. An equilibrium band diagram of a symmetric M_1IM_1 tunnel device is shown in Fig. 6.6a. The *J–V* characteristic of a symmetric M_1IM_1 device is expected to be symmetric because the barrier to electron tunneling is equivalent in either direction. However, the diodes investigated in this chapter have asymmetric electrodes. An equilibrium band diagram of an asymmetric M_1IM_2 tunnel diode is shown in Fig. 6.6b. φ_{b1} and φ_{b2} indicate the barrier height of the bottom electrode metal M_1 (Ir, Pt, or ZrCuAlNi) and the smaller work function top gate electrode metal M_2 (Al), respectively. Additional band diagrams of the asymmetric diode show (c) the onset of FN tunneling for a positive bias applied to M_2 and (d) direct tunneling for the same absolute magnitude negative bias applied to M_2. The last two band diagrams illustrate the origin of the expected asymmetry in M_1IM_2 devices.

Consider first the application of a sufficiently large *positive* bias to electrode M_2 (Al), so that FN tunnel emission occurs from M_1 (Ir, Pt, or ZrCuAlNi). This situation is illustrated in energy band diagrams shown in Fig. 6.7a–c which depict the applied bias at which tunnel emission from electrode M_1 transitions from direct tunneling (through the entire insulator thickness) to FN tunneling (through a triangular shape barrier in which the tunnel distance decreases further with increasing bias). Since the insulator thickness (~10 nm) is sufficient to suppress direct tunneling, current conduction is dominated by FN tunneling. As indicated in (6.1), the magnitude of the FN tunneling current depends on the inverse exponential of *S* and the square root of cube of the barrier height presented to the tunneling electron ($J \propto \exp(-S\varphi_b^{3/2})$). Thus, while the *onset* of FN tunneling at positive bias

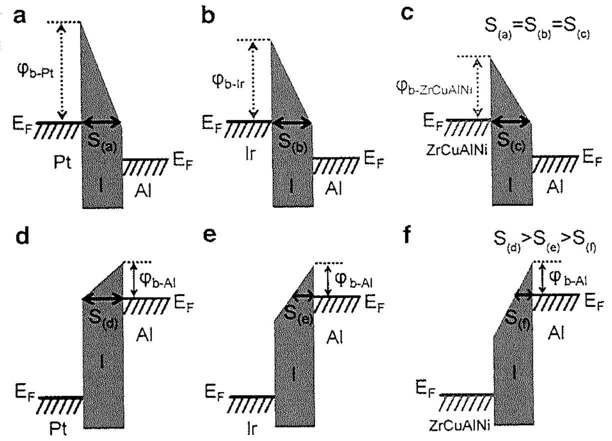

Fig. 6.7 Band diagrams of M_1IM_2 diodes with different *bottom* M_1 electrodes under (**a–c**) a positive bias of φ_{b-Al}/q and (**d–f**) a negative bias of φ_{b-Pt}/q. In all band diagrams, the left electrode (M_1) is grounded and voltage is applied to the Al electrode (M_2). Two important parameters in tunneling probability are shown for each band diagram. For the same applied positive bias in (**a–c**), *S* is the same for all devices, but φ_b is dependent on the Pt, Ir, and ZrCuAlNi bottom electrode. For the same negative applied bias in (**d–e**), φ_b is the same for all devices while *S* is dependent upon the Pt, Ir, and ZrCuAlNi bottom electrode

will be roughly the same for all bottom electrodes (as it involves overcoming the same barrier height, φ_{Al}, of the Al top electrode as shown in Fig. 6.7a–c), the magnitude of the FN tunneling current at larger positive fields ($V_{app} \gg \varphi_{b2}$) should be in reverse order of increasing φ_{b1} (increasing Φ_{M1}). Based on relative φ_{b1}, it is expected that a diode with the ZrCuAlNi electrode ($\Phi_{ZrCuAlNi} = 4.8$ eV) should show the highest current density, the Ir electrode ($\Phi_{Ir} = 5.1$ eV) should show the next highest current density, and that the devices with the Pt electrodes ($\Phi_{Pt} = 5.3$ eV) should show the lowest current density. This trend is observed in the simulations (Fig. 6.5a). Although the ZrCuAlNi bottom electrode device is well predicted by simulation, decreased current density with increased Φ_{M1} is clearly not the trend exhibited by the experimental data (Fig. 6.5b) [2].

Assuming that the Al_2O_3 thickness is the same for all devices and that conduction is dominated by FN tunneling, a likely explanation for the unexpected trend shown by the data in Fig. 6.5b is associated with the relative roughness of the bottom electrode. A rough bottom electrode could lead to electric field nonuniformity across the insulator due to field enhancement at nm scale sharp features [50, 51]. This field enhancement would result in locally increased conduction [3]. As listed in Table 6.1 and illustrated in Fig. 6.3, Ir showed the largest as-deposited RMS roughness (11 nm) followed by e-beam deposited Pt-2 (6 nm), sputtered Pt-1 (2 nm), and finally ZrCuAlNi (0.3 nm). Looking again at Fig. 6.5b, it is apparent that increasing positive polarity current density correlates with increasing bottom electrode roughness, rather than with decreasing Φ_{M1}. As the RMS roughness for both Ir and Pt-2 is comparable to the overall dielectric

thickness, it is not surprising that bottom electrode roughness overwhelms the expected influence of Φ_{M1}. A clear indication of the impact of roughness can be seen by directly comparing MIM tunnel diodes made using the *same* bottom electrode metal (Pt) with two different levels of roughness. As seen in Fig. 6.5b, despite what should be nominally the same Φ_M, the rougher (RMS = 6 nm) e-beam evaporated Pt-2 device shows a higher positive bias current density than the smoother (RMS = 2 nm) DC sputtered Pt-1 device.

Considering now the application of a sufficiently large *negative* bias to electrode M_2 so that FN emission occurs from M_2 (Al). As indicated in the energy band diagrams in Fig. 6.7d–f, for larger φ_{b1}, the onset of FN tunneling should require application of larger negative voltages. The simulations in Fig. 6.5a are consistent with this expectation. After the onset of FN tunneling at negative bias, since the barrier height of the emission electrode is nominally the same for all devices as shown in Fig. 6.7d–f, the *I–V* curves of all devices should exhibit roughly the same slope. Once again, the devices made with ZrCuAlNi as a bottom electrode match fairly well with simulation (Fig. 6.5). As compared with the simulation, the voltage required to achieve a given current density is reduced only slightly for both the Pt and Ir electrode devices. Ir shows the greatest deviation from simulation while the rougher Pt-2 once again deviates more than Pt-1.

The deviation between measured and simulated current density is much less on the negative bias side than on the positive bias side (Fig. 6.5). Additional FN tunneling simulations show that in an asymmetric M_1IM_2 device, tunnel emission from the higher work function M_1 (the situation at positive bias) is more sensitive to changes in the tunnel barrier (such as in thickness, electron effective mass, or electron affinity) than tunneling from the lower work function side M_2 (the situation at negative bias). The data in Fig. 6.5 suggests that tunneling from the higher work function M_1 side (again, positive bias in these experiments) is also more sensitive to roughness than tunneling from the smaller work function side (negative bias in these experiments).

Desired J–ξ characteristics for diodes include high f_{NL} and high η_{asym}. As illustrated by the simulations in Fig. 6.8a, assuming that FN tunneling dominates conduction, a larger $\Delta\Phi_M$ between electrodes should lead to higher maximum η_{asym} (η_{max}) so that the Pt (largest Φ_M) device should show the highest η_{max} and the ZrCuAlNi device (lowest Φ_M) the lowest η_{max}. Because of the smaller energy barrier heights, the ZrCuAlNi bottom electrode device would be expected to show asymmetric response at the lowest bias.

As shown in Fig. 6.8b, this trend was not observed. The largest η_{max} for the actual devices is associated with the ZrCuAlNi electrode device, the device with the smoothest M_1. Clearly opposite to expectations, the devices with rough Pt and Ir bottom electrodes show asymmetry of *reverse* polarity to what was predicted. The qualitative *J–V* response of the Pt and Ir devices, higher current for positive bias than for negative bias, means that a larger tunneling current is flowing from the larger tunnel barrier electrode. This cannot be explained by the FN tunneling equation in (6.1). However, this situation may be explained by electrode roughness. Choi et al. [3] have shown that the tunneling probability may be

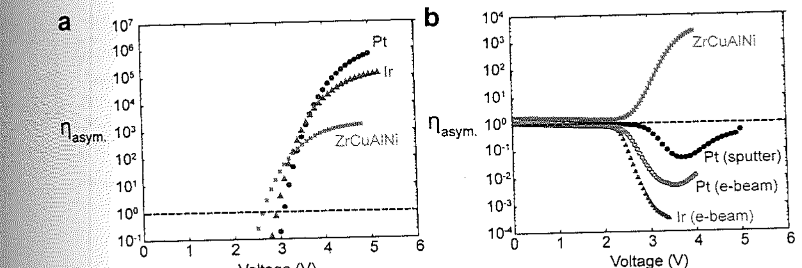

Fig. 6.8 (**a**) Simulated and (**b**) experimental plots of log (η_{asym}) vs. *V*, for MIM diodes with either ZrCuAlNi, Ir, or Pt bottom electrodes, 10 nm Al_2O_3, and Al top electrodes where asymmetry $\eta_{asym} = |I_-/I_+|$

enhanced by electrode geometry. They report geometric electric field enhancement, in which one of the electrodes is deliberately fabricated with a sharp geometry, produced an asymmetric *I–V* response in an otherwise electrically symmetric MIM device with Ni top and bottom electrodes. In our experiments, it appears that geometry enhanced asymmetry is seen for devices with the rough Pt and Ir electrodes. In fact, as shown in Fig. 6.8b, the asymmetric response of diodes made with rough bottom electrodes is correlated with the roughness. Diodes made with largest RMS roughness bottom electrode (Ir) show the largest reversed asymmetry values followed by the Pt-2 (e-beam) and the Pt-1 (sputtered) devices. It appears that the full extent of $\Delta\Phi_M$ induced asymmetry can be realized only if the roughness of the larger work function electrode is minimized.

Bottom electrode (M_1) roughness was also found to be inversely correlated with the percentage of functioning MIM diodes. Diodes were considered nonfunctioning due to either electrical shorts or early breakdown under a low applied electric field. It is seen in Table 6.1 that smoother bottom electrodes were found to yield a greater percentage of functioning devices. Devices fabricated using ZrCuAlNi, the smoothest bottom electrode investigated, have the highest fraction of functioning devices. At the opposite end of the roughness spectrum, the Al films were the roughest metal films investigated, with a post-ALD RMS roughness of 21 nm (greater than the tunnel barrier thickness) and a peak roughness of more than 450 nm. It is not surprising that no functioning diodes could be obtained using Al bottom electrodes. Comparing the two types of Pt, use of the smoother Pt-1 resulted in a higher percentage of functioning devices than the rougher Pt-2 devices. Finally, despite lower as-deposited and roughly equivalent post-ALD RMS roughness, Pt-2 bottom electrodes are found to yield a lower percentage of working devices than Ir bottom electrodes. This appears to be due to the larger peak roughness of the Pt-2 electrode devices.

Using the ultra-smooth ZrCuAlNi as M_1, uniform and repeatable device characteristics were produced with high yield that are well predicted by FN tunneling theory and the Simmons equations. Shown in Fig. 6.9a are J–ξ curves for seven Al top electrode (M_2)/~10 nm thick Al_2O_3 tunnel barrier/ZrCuAlNi (M_1)

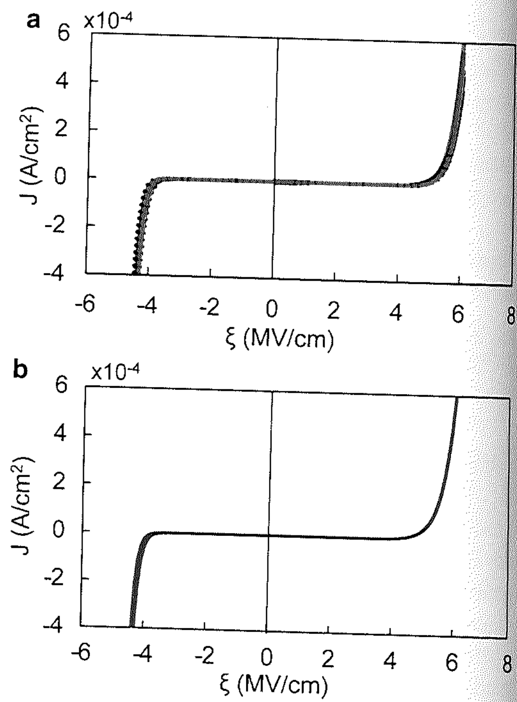

g. 6.9 (a) J–ξ sweeps for ...ven different MIM tunnel ...odes taken from five ...fferent substrates ...ricated in four different ...ntical process runs. ...fferent shades indicate ...ferent devices. The fact ...t the devices overlap and ... barely distinguishable ...m one another is an ...ication of the run to run ...l device to device ...formity. (b) Hundred ...uential J–ξ sweeps on a ...gle device. In all cases, the ...k structure of the devices ...sists of ZrCuAlNi/ ... nm Al_2O_3/Al. Adapted ...n [6]

...des from five different substrates produced in four different process runs. Note ... despite the inverse dependence of yield on bottom electrode roughness and ...-agreement with FN theory for the rough bottom electrode devices, when ...*tioning* devices are obtained, even the devices with rough bottom electrode ...Pt-1, and Pt-2) exhibit little variation in J–ξ characteristics.

...hown in Fig. 6.9b are 100 sequential J–ξ sweeps (−4.5 V to +6 V to −4.5 V) on ...CuAlNi M_1/~10 nm thick Al_2O_3 tunnel barrier/Al M_2 device showing stable ...response. Further reliability investigations described in [6] have shown that ...ces with rougher bottom electrodes are more susceptible to failure due to bias ...sing. Finally, we have also observed that increased bottom electrode roughness ...orrelated with increased I–V hysteresis in these devices, suggesting that ...ased roughness may lead to increased charge trap density, which in turn ...d lead to energy barrier height variations.

... Step Tunneling Enhanced Asymmetry in MIIM Diodes

...is section, the combined effect of bilayer tunnel barriers and asymmetric ...$\neq \Phi_{M2}$) electrodes are investigated on $M_1I_1I_2M_2$ diodes fabricated ... atomically smooth ZrCuAlNi amorphous metal bottom electrodes and

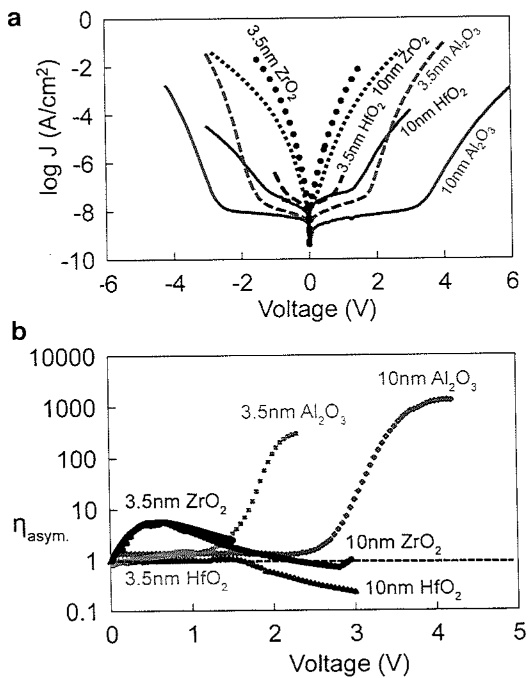

Fig. 6.10 Plots of (a) log (J) vs. V and (b) log (η_{asym}) vs. V for single dielectric M_1IM_2 devices

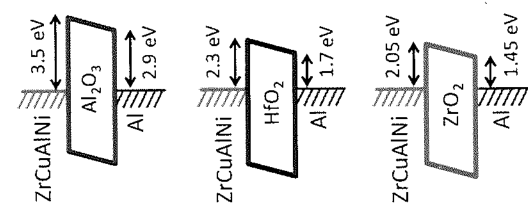

Fig. 6.11 Estimated equilibrium band diagrams for Al_2O_3, HfO_2, and ZrO_2 M_1IM_2 diodes where M_1 = ZrCuAlNi and M_2 = Al

nanolaminate dielectric bilayers of HfO_2/Al_2O_3 and ZrO_2/Al_2O_3 deposited via ALD [11].

Shown in Fig. 6.10 are plots of (a) log (J) vs. V and (b) log (η_{asym}) vs. V comparing the single layer M_1IM_2 diodes with ZrCuAlNi bottom electrodes (M_1) and Al top gates (M_2) where the I is a single 3.5 nm or 10 nm layer of either Al_2O_3, HfO_2, or ZrO_2. As expected, current density is a rough function of the relative barrier heights, as shown in the band diagrams in Fig. 6.11. In Fig. 6.10a the dominance of FN tunneling is apparent from the presence of the "knees" in the log (J)–V data at positive and negative bias that are followed by several orders of magnitude of exponentially increasing current. Not shown, FN plots of ln $(I/(V + \Delta\Phi)^2)$ vs. $1/(V + \Delta\Phi)$ indicate that Al_2O_3 and HfO_2 devices are dominated by FN tunneling in the post-turn-on regime. The ZrO_2 devices, on the other hand, appear to be dominated by thermionic emission. Due to the $\Delta\Phi_M$

John F. Conley

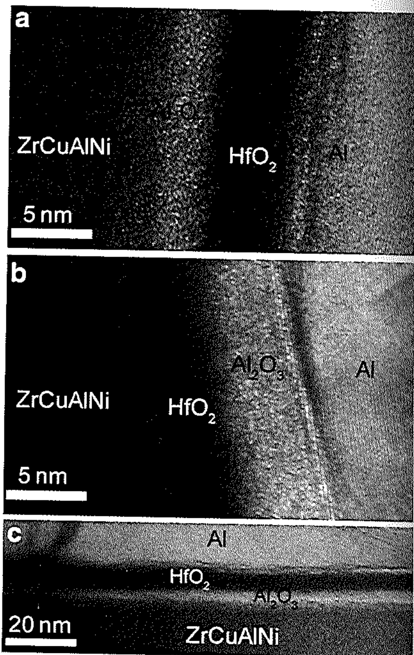

Fig. 6.12 High magnification cross sectional transmission electron microscopy (TEM) images of (**a**) ZrCuAlNi/Al_2O_3/HfO_2/Al $M_1I_1I_2M_2$ and (**b**) ZrCuAlNi/HfO_2/Al_2O_3/Al $M_1I_2I_1M_2$ devices. A lower magnification TEM image of the ZrCuAlNi/Al_2O_3/HfO_2/Al $M_1I_1I_2M_2$ device is shown in (**c**)

etween the top and bottom electrodes, the devices are expected to show asymmetry. In Fig. 6.10b, it is seen that the 10 nm Al_2O_3 diode shows a η_{max} of pproximately 1,350 at 4.1 V. Although the Al_2O_3 devices show excellent η_{asym} at igher biases, for many applications, including energy harvesting, asymmetric peration at low voltage is desirable. As seen in Fig. 6.10b, decreasing the tunnel arrier thickness to 3.5 nm resulted in decreased turn-on voltages and increased urrent for all devices. However η_{max} was not improved, most likely due to the ncreased influence of direct tunneling. Decreasing the thickness of the single nsulator layer in an M_1IM_2 diode does not lead to improved asymmetry.

In order to create an asymmetric tunnel barrier, Al_2O_3 and HfO_2 were stacked to orm bilayer insulator MIIM devices. Cross sectional TEM images of ZrCuAlNi/ l_2O_3/HfO_2/Al $M_1I_1I_2M_2$ devices and ZrCuAlNi/HfO_2/Al_2O_3/Al $M_1I_2I_1M_2$ evices are shown in Fig. 6.12. For each dielectric bilayer, 56 ALD cycles were sed to deposit Al_2O_3 and 65 cycles were used to deposit HfO_2, targeting a hickness of 5 nm for each layer. The high magnification TEM images in (a) and) show that the thickness of the *top* dielectric layer is indeed approximately equal the 5 nm target. However, in each case, the thickness of the bottom dielectric yer deposited directly on the ZrCuAlNi bottom electrode is only approximately .5 nm. This reduced thickness is likely due to an inhibition of the ALD nucleation te on ZrCuAlNi as compared to that on oxide. Also visible in the high resolution EM images is the presence of an approximately 2 nm thick interfacial layer etween the ZrCuAlNi and the bottom dielectric. This interfacial layer was reviously determined to be composed of ZrO_x [2]. In Fig. 6.12c, a lower

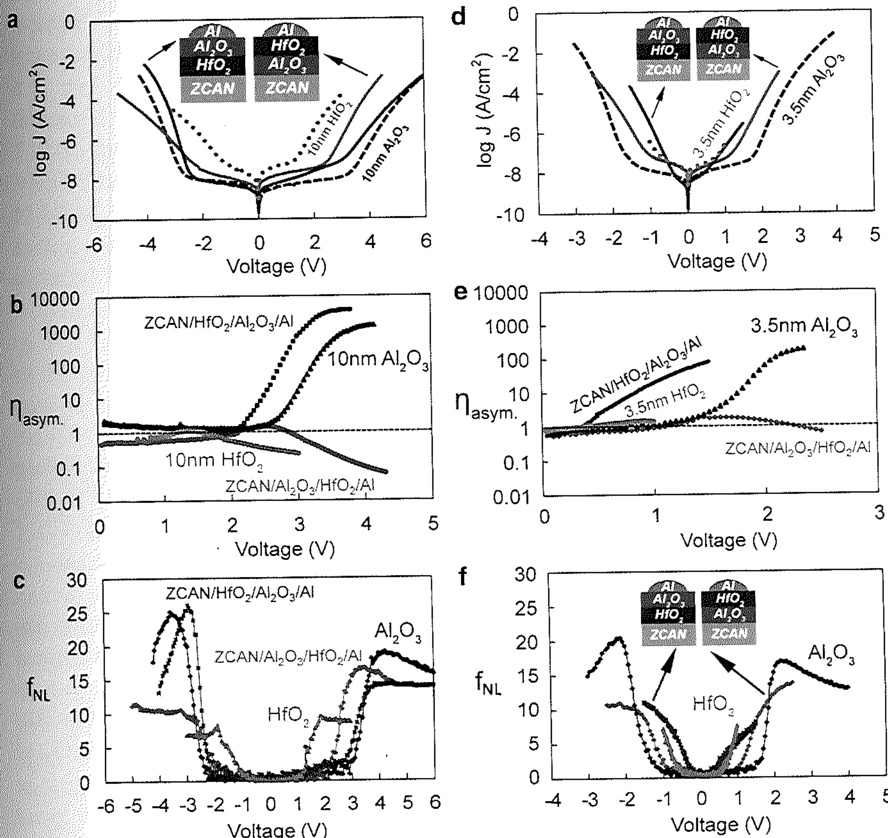

Fig. 6.13 Shown are (**a**) log (J) vs. V, (**b**) log (η_{asym}) vs. V, and (**c**) f_{NL} vs. V plots for "thick" bilayer ZrCuAlNi/3.5 nm Al_2O_3/5 nm HfO_2/Al $M_1I_1I_2M_2$ and ZrCuAlNi/3.5 nm HfO_2/5 nm Al_2O_3/Al $M_1I_2I_1M_2$ diodes. Included for reference are the 10 nm thick single dielectric Al_2O_3 and HfO_2 M_1IM_2 diodes from Fig. 5.10. Also shown are (**d**) log (J) vs. V, (**e**) log (η_{asym}) vs. V, and (**f**) f_{NL} vs. V plots for "thin" bilayer ZrCuAlNi/Al_2O_3/HfO_2/Al $M_1I_1I_2M_2$ and ZrCuAlNi/HfO_2/Al_2O_3/Al $M_1I_2I_1M_2$ diodes. Al_2O_3 and HfO_2 layers were deposited using 28 and 32 ALD cycles, respectively. M_1IM_2 diodes with 3.5 nm layers of either Al_2O_3 or HfO_2 are included for comparison

magnification image of the device from (a), reveals the smooth nature of the ZrCuAlNi/Al_2O_3 interface over an extended range. As discussed above in Sect. 6.3, a smooth bottom interface is critical to achieving high yield, high quality MIM tunnel devices [1, 6].

Figure 6.13 shows (a) log (J) vs. V, (b) log (η_{asym}) vs. V, and (c) f_{NL} vs. V plots for ZrCuAlNi/3.5 nm Al_2O_3/5 nm HfO_2/Al $M_1I_1I_2M_2$ and ZrCuAlNi/3.5 nm HfO_2/ 5 nm Al_2O_3/Al $M_1I_2I_1M_2$ diodes. Included for reference are the 10 nm thick single dielectric Al_2O_3 and HfO_2 M_1IM_2 diodes from Fig. 6.10.

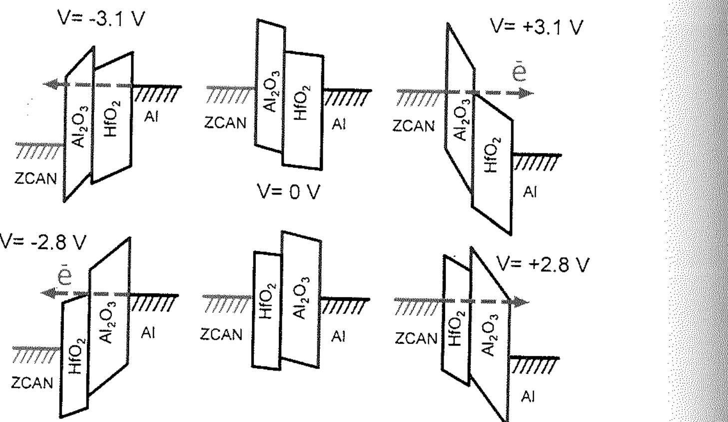

Fig. 6.14 Band diagrams illustrating (**a**) ZrCuAlNi/3.5 nm Al_2O_3/5 nm HfO_2/Al $M_1I_1I_2M_2$ diodes and (**b**) ZrCuAlNi/3.5 nm HfO_2/5 nm Al_2O_3/Al $M_1I_2I_1M_2$ diodes under negative bias (*left*), equilibrium (*center*), and positive bias (*right*). In all band diagrams, the left electrode (M_1) is grounded and voltage is applied to the Al electrode (M_2)

The inherent asymmetry of these dual dielectric barriers is evident in the equilibrium band diagrams shown in Fig. 6.14. Differences in the electrical behavior are qualitatively explained by the nonequilibrium band diagrams, which illustrate the approximate onset of step tunneling at positive bias for the ZrCuAlNi/Al_2O_3/HfO_2/Al device and at negative bias for the ZrCuAlNi/HfO_2/Al_2O_3/Al device, respectively. The "onset of step tunneling" refers to the applied bias at which the E_F in the electron emitting metal rises just above the E_C of the lower barrier HfO_2 so that tunneling may occur through only the larger barrier Al_2O_3 layer.

Considering first the ZrCuAlNi/Al_2O_3/HfO_2/Al $M_1I_1I_2M_2$ device, in which the larger E_G Al_2O_3 layer (I_1) is adjacent to the larger Φ_{M1} ZrCuAlNi electrode, application of approximately +3.1 V (Fig. 6.14 top, right) brings the Fermi level of the ZrCuAlNi to just above the conduction band of the HfO_2 so that direct tunneling may occur from left to right through only the 3.5 nm thick Al_2O_3 layer—a step reduction in the minimum required tunnel distance. For application of an opposite polarity −3.1 V bias (Fig. 6.14 top, left) electrons tunneling from right to left at the Fermi level must pass through both insulating layers. Therefore, a larger current is expected for positive bias than for an equivalent magnitude negative applied bias and $\eta_{asym} < 1$ is expected. This expectation of $\eta_{asym} < 1$ is confirmed in Fig. 6.13b. Note that the direction of the asymmetry ($\eta_{asym} < 1$) for the ZrCuAlNi/Al_2O_3/HfO_2/Al device is reverse that of the single Al_2O_3 layer device ($\eta_{asym} > 1$), indicating that the asymmetry of the bilayer dielectric barrier not only *opposes* that of the built-in voltage induced by $\Delta\Phi_M$, but overwhelms its impact on device operation. As seen in equation (6.1), the tunnel current is exponentially dependent upon $\varphi_b^{-3/2}$. Since $\varphi_{Al\text{-}HfO_2} < \varphi_{ZrCuAlNi-Al_2O_3}$, at higher magnitude applied biases the negative bias current (tunneling from Al) will begin to

increase more rapidly than the positive bias current (tunneling from ZrCuAlNi) and it is expected that the slope of the log (η_{asym})–V plot will decrease [38]. In Fig. 6.13b it is seen that for application of +4 V, the slope of the log (η_{asym})–V plot has decreased.

Also shown are (d) log (J) vs. V, (e) log (η_{asym}) vs. V, and (f) f_{NL} vs. V plots for "thin" bilayer ZrCuAlNi/Al_2O_3/HfO_2/Al $M_1I_1I_2M_2$ and ZrCuAlNi/HfO_2/Al_2O_3/Al $M_1I_2I_1M_2$ diodes. Al_2O_3 and HfO_2 layers were deposited using 28 and 32 ALD cycles, respectively. M_1IM_2 diodes with 3.5 nm layers of either Al_2O_3 or HfO_2 are included for comparison.

Considering next the *reverse insulator stack orientation* ZrCuAlNi/HfO_2/Al_2O_3/Al $M_1I_2I_1M_2$ device, in which the larger band-gap Al_2O_3 layer (I_1) is now adjacent to the smaller Φ_{M2} Al electrode. With −2.8 V applied to the Al gate (Fig. 6.14 bottom, left), the Fermi level in the Al gate lies just above the conduction band of the HfO_2 and electrons injected from the Al (M_2) may tunnel directly through only the Al_2O_3 layer (a step reduction in tunnel distance). On the other hand, for +2.8 V applied to the Al gate (Fig. 6.14 bottom, right) electrons injected from the ZrCuAlNi (M_1) must pass through both dielectric layers. Therefore, a smaller current is expected at positive bias than at an equivalent magnitude negative bias so that $\eta_{asym} > 1$ is expected. This expectation is also confirmed in Fig. 6.13b. In this case bilayer dielectric barrier *enhances* the electrode $\Delta\Phi_M$ asymmetry and η_{asym} is *increased* over that of the single Al_2O_3 layer M_1IM_2 diode. Since $\varphi_{Al-Al_2O_3} > \varphi_{ZrCuAlNi-HfO_2}$, as the magnitude of the applied bias increases, the current density will begin to increase more quickly under positive bias (injection from ZrCuAlNi) than negative bias (injection from Al) and the slope of the η_{asym}–V plot will be expected to decrease. This expectation is confirmed in Fig. 6.13b.

Shown in Fig. 6.13c, it is seen that all devices exhibit excellent f_{NL} with the bilayer ZrCuAlNi/HfO_2/Al_2O_3/Al $M_1I_2I_1M_2$ diode showing the highest maximum nonlinearity ($f_{NL\text{-}max} \sim 27$). Consistent with its enhanced η_{asym}, this device also shows enhanced f_{NL} at low negative bias exceeding that of the single layer Al_2O_3 and HfO_2 devices. The reverse orientation ZrCuAlNi/Al_2O_3/HfO_2/Al device shows improved f_{NL} over the single layer Al_2O_3 diode at low positive bias and reduced f_{NL} at negative bias, consistent with the direction of its η_{asym}. The single layer HfO_2 device shows the best f_{NL} below ~$|2V|$, due to its lower turn-on voltage. The appearance of the sharp increase in f_{NL} for both bilayer devices is at the bias and polarity expected for step tunneling (based on the band diagram simulations in Fig. 6.14).

Also shown in Fig. 6.13 are (d) log (J) vs. V, (e) log (η_{asym}) vs. V, and (f) f_{NL} vs. V plots for *thinner* dielectric bilayer ZrCuAlNi/Al_2O_3/HfO_2/Al $M_1I_1I_2M_2$ and ZrCuAlNi/HfO_2/Al_2O_3/Al $M_1I_2I_1M_2$ diodes. The HfO_2 and A_2O_3 layers in these devices were deposited using 32 and 28 ALD cycles, respectively. The estimated thicknesses of the bottom and top dielectric layers are ~1 and ~2.5 nm, respectively. For reference, also plotted are the thinner single dielectric layer Al_2O_3 and HfO_2 M_1IM_2 diodes from Fig. 6.10, which were deposited using 56 and 65 ALD cycles, respectively. Qualitatively, the behavior of the thinner bilayer devices is similar to

the thicker devices, but in all cases η_{max} is reduced—behavior that was also seen for the single layer MIM devices. Once again for the ZrCuAlNi/Al_2O_3/HfO_2/Al $M_1I_1I_2M_2$ device, the dual dielectric bilayer *opposes* the work function induced asymmetry. At voltages greater than about 2.5 V, $\eta_{asym} < 1$, opposite to the $\eta_{asym} > 1$ of the single layer Al_2O_3 device. For the reverse orientation ZrCuAlNi/ HfO_2/Al_2O_3/Al $M_1I_2I_1M_2$ device, the asymmetry induced by the different electrode work functions is once again *enhanced* by the bilayer dielectric tunnel barrier, esulting in an η_{asym} of higher magnitude than that of the single layer Al_2O_3 device.

The reduced tunnel barrier thickness, as seen in Fig. 6.13f, resulted in improved $_{NL}$ at small biases for all devices. This is due primarily to the lower turn-on oltages and higher conductivity (compare Fig. 6.13a, b). Note however that the nprovement for the bilayer devices is even greater than for the single layer evices. As compared to single layer Al_2O_3, both of the thin MIIM devices now now enhanced low bias f_{NL} for both polarities. Again, both bilayer devices have eir highest f_{NL} for the bias polarity at which the step reduction in tunneling stance occurs. Consistent with the η_{asym} data, for the ZrCuAlNi/Al_2O_3/HfO_2/Al $_1I_1I_2M_2$ devices f_{NL} is highest at positive bias, while for ZrCuAlNi/HfO_2/Al_2O_3/ l $M_1I_2I_1M_2$ devices f_{NL} is highest at negative bias.

Note that for rectenna applications, MIM rectifying diodes must match the npedance of the antenna. As small device areas are required to minimize pacitance for high speed operation, ultrathin diodes will be needed in order to ovide a sufficiently low resistance to match the impedance of antennas (~100 Ω). e fact that the MIIM devices appear to scale better than single layer MIM diodes ggests they are an excellent candidate for rectenna applications.

Overall, the thin bilayer ZrCuAlNi/HfO_2/Al_2O_3/Al device, despite reduced η_{max} l $f_{NL\text{-}max}$ as compared to the single layer Al_2O_3 device, shows excellent low tage characteristics with $\eta_{asym} > 10$ and $f_{NL} > 5$ at voltages as low as 0.8 V. y recent work has shown that insulator heterojunctions can be used to produce mmetric *I–V* behavior in symmetric metal electrode $M_1I_1I_2M_1$ diodes, devices in ch the same metal is used for the top and bottom electrodes [5, 9, 10]. As a point eference, Maraghechi et al. [5], recently reported $\eta_{asym} \sim 10$ at 3 V and < 5 at 0.8 V for a symmetric electrode Cr/2 nm HfO_2/2 nm Al_2O_3/Cr diode. t is clear that dielectric bilayers can have a significant impact on M_1IIM_2 device ation. Examining more closely the ZrCuAlNi/Al_2O_3/Al band diagram in 6.11 and only considering asymmetry due to tunneling-based conduction, the t of the tunneling-based asymmetry should begin at roughly the same voltage, oendent of insulator thickness. However, in Fig. 6.10b it is seen that while ficant asymmetry appears above about 3 V in the 10 nm Al_2O_3 device, ficant asymmetry occurs above about 2 V in the 3.5 nm Al_2O_3 device. One ble explanation for this discrepancy is the thin ZrO_x interfacial layer (IL) een the ZrCuAlNi electrode and the overlying dielectric (see Fig. 6.12 and also Because of this IL, even the nominally single layer devices might be, in fact, er devices. To model the potential impact of the ZrO_x IL, band diagrams ar to those in Fig. 6.14(bottom row) may be used, replacing HfO_2 with 2 nm of and using an Al_2O_3 thickness of either 3.5 or 10 nm. For both ZrCuAlNi/2 nm

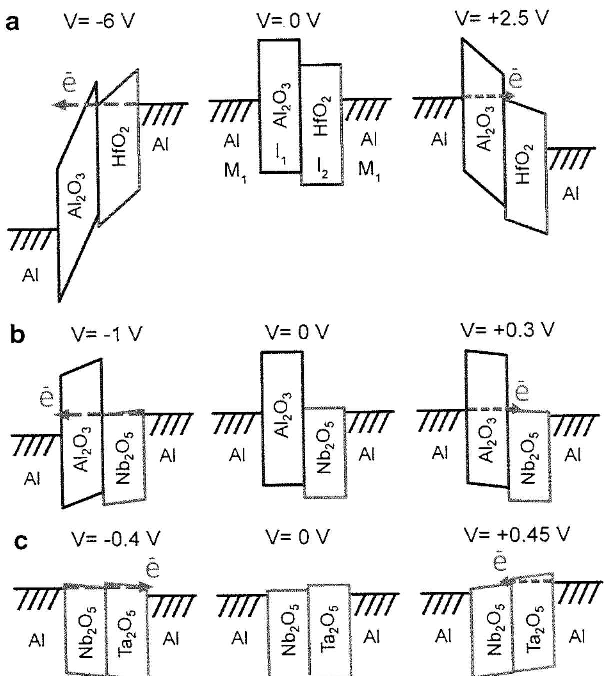

Fig. 6.15 Simulated energy band diagrams of $M_1I_1I_2M_1$ symmetric electrode tunnel diodes, showing step tunneling (*right*) and resonant tunneling (*left*) for a variety of bilayer dielectric stacks with equal thickness layers. In all band diagrams, left electrode is grounded and voltage is applied to right electrode

ZrO_x IL/Al_2O_3/Al bilayer devices, the minimum voltage required for the step reduction in tunneling distance is simulated to be approximately 2.25 V. However, in the thicker device, the electrons must tunnel through a 10 nm thick Al_2O_3 layer while in the thinner device, the electrons have to tunnel through only an approximately 3.5 nm thick Al_2O_3 layer. As seen in (6.1), tunneling current is exponentially dependent upon the inverse of the barrier thickness ($I \propto e^{-S}$) [38]. Thus in the presence of the ZrO_x IL, the onset voltage for tunneling-based asymmetry is expected to be reduced as the thickness of the Al_2O_3 layer is reduced. Looking again at the single layer Al_2O_3 devices in Fig. 6.10, it seems evident that *I–V* characteristics and η_{asym} were impacted by the presence of the ZrO_x IL, although it is also possible that an emission-based conduction mechanism [8] or barrier lowering in the ultrathin device structure, not considered here, may play a role. The IL layer likely plays a role in the nominally single layer HfO_2 device as well, but since the E_G and χ of HfO_2 are likely similar to the E_G and χ of the ZrO_x IL, its impact is more difficult to predict. For the single layer ZrO_2 device, the ZrO_x IL layer appears to have little impact.

It should be noted that only step tunneling is of concern to this work. For the dielectrics used in this study, resonant tunneling is not relevant. Simulations were performed for a variety of dielectric bilayer stacks with wide and narrow band-gaps. Shown in Fig. 6.15 are representative simulated band diagrams for various stacks showing the minimum voltage required for resonant tunneling and for step

ig. 6.16 J–V plots for $M_1I_1I_2M_2$ diodes made with rCuAlNi *bottom* and Al *top* lectrodes. The tunnel barrier onsists of either a single yer of Al_2O_3, a single layer f ZrO_2, or various Al_2O_3/ rO_2 I_1/I_2 bilayers. In all ases, the total thickness of e tunnel barrier is 10 nm

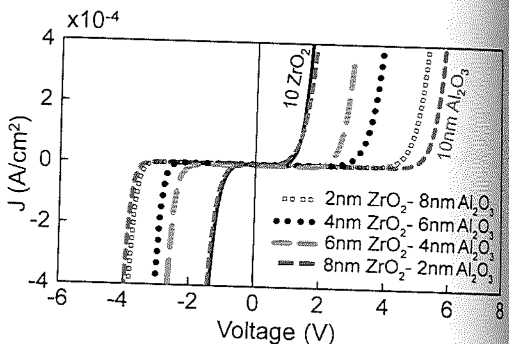

nneling. To present a simplified picture, symmetric work function electrodes were sumed. It was found that for almost all bilayer stacks of SiO_2, Al_2O_3, HfO_2, ZrO_2, a_2O_5, Nb_2O_5, and TiO_2, step tunneling occurs at a smaller absolute bias than sonant tunneling. The only exception was the Nb_2O_5/Ta_2O_5 bilayer stack shown Fig. 6.15c, in which resonant tunneling is predicted to occur at a lower bias than ep tunneling, consistent with recent simulation work on tunneling probability [9,]. As shown in Figs. 6.14 and 6.15, for the bilayer stacks used in this study, the ectric field required to reach resonant tunneling exceeds the breakdown strength the constituent HfO_2, Al_2O_3, and ZrO_2 dielectrics.

Finally, shown in Fig. 6.16 is a J–V plot of ZrCuAlNi bottom electrode devices th Al top electrodes. In all cases, the total thickness of the tunnel barrier is 10 nm d consists of either a single layer of Al_2O_3, a single layer of ZrO_2, or various $_2O_3/ZrO_2$ I_1/I_2 bilayers. From this preliminary data, it is seen that relative ckness of the individual insulator layers in the bilayer stack may be used to ther tune electrical behavior.

Summary

ereas most previous experimental work on MIM diodes has been conducted on ve oxides produced by either oxidation or nitridation of the bottom metal trode, the use of ALD in this work allowed deposition of high quality single r and nanolaminate bilayer insulators independent of the bottom metal trode material. Using these high quality ALD insulators, the impact of bottom trode roughness on M_1IM_2 diode performance and the impact of nanolaminate lator bilayers on $M_1I_1I_2M_2$ diode performance were explored.

n the first half of the chapter, the performance of MIM tunnel diodes with ALD O_3 insulator tunnel barriers on low work function (ZrCuAlNi and Al) and high k function (Ir and two types of Pt) bottom electrode materials with RMS roughness ls ranging from ~3 % to greater than 100 % of the insulator thickness was stigated. It was demonstrated that the roughness at the bottom metal interface can overwhelm the influence of metal work function on the electrical characteristics of M_1IM_2 diodes, even reversing the trends expected based on $\Delta\Phi_M$. It was also shown that the percentage yield of functioning devices tracks higher with decreasing roughness and that even for nominally the same metal (Pt), the level of roughness dominates electrical properties and yield. These results indicate that bottom electrode roughness levels of much less than 20 % of the insulator thickness are necessary to achieve non-roughness dominated electrical behavior, suggesting that many previous MIM tunnel diode studies may have been compromised by uncontrolled bottom electrode roughness [19–24, 27–34]. By combining uniform tunnel barriers deposited via ALD with ultra-smooth (~0.3 nm RMS) ZrCuAlNi amorphous metal bottom electrodes, highly nonlinear and asymmetric MIM tunnel diodes with good device to device uniformity and stable J–V behavior have been demonstrated.

For rectenna-based solar cells as well as other potential applications of MIM diodes, highly asymmetric and highly nonlinear I–V behavior at low applied voltages is required. The standard approach to achieving asymmetric I–V characteristics in tunnel devices is to make M_1IM_2 diodes using metals with different work functions ($\Phi_{M1} \neq \Phi_{M2}$) so as to produce a built-in field across the tunnel barrier [6, 40]. Unfortunately, the amount of asymmetry achievable using the metal work function approach is limited by the $\Delta\Phi_M$ that can be obtained using practical electrodes. Note that ultra-smooth amorphous metals such as ZrCuAlNi, despite multiple metal components, typically do not allow a broad tuning of their electrical properties such as work function [53, 54].

Therefore, in the second half of this chapter, an additional approach to achieving asymmetric and nonlinear operation is investigated in which a nanolaminate pair of insulators (each with different E_G and χ) are used to create asymmetric tunnel barrier MIIM devices. In MIIM devices, electrons tunneling from one metal electrode to the other are presented with a different barrier shape depending on the direction of tunneling. It was demonstrated that high quality nanolaminate bilayer tunnel barriers deposited via ALD dominate the electrical characteristics of asymmetric metal electrode M_1IIM_2 devices. I–V asymmetry and nonlinearity were found to be sensitive to the arrangement of the individual insulator layers with respect to the different metal electrodes ($M_1I_1I_2M_2$ vs. $M_1I_2I_1M_2$). Depending on whether the smaller χ insulator was adjacent to the smaller or larger Φ_M electrode, respectively, the bilayer dielectrics were arranged to either enhance or oppose (even reverse) the $\Delta\Phi_M$ induced asymmetry. Using band diagrams and assuming that conduction is dominated by tunneling mechanisms, these results are qualitatively well explained by step tunneling (Figs. 6.14 and 6.15). By combining two methods of producing asymmetry, asymmetric metal electrodes and a bilayer dielectric tunnel barrier, we were able to achieve excellent low voltage asymmetry and nonlinearity in a ZrCuAlNi/HfO_2/Al_2O_3/Al diode exceeding both that of standard single dielectric layer asymmetric electrode M_1IM_2 devices as well as recently reported symmetric electrode $M_1I_1I_2M_1$ devices. Finally, it was also demonstrated that the relative thickness of the insulator layers may be used to further tune electrical behavior.

Overall, it was shown that combining uniform tunnel barriers deposited via ALD
n ultra-smooth metal bottom electrodes, allows for the fabrication of
vler–Nordheim tunneling dominated MIM devices. It was also clearly
erimentally demonstrated that nanolaminate insulator tunnel barriers are a
verful way to enhance or tune the asymmetry and nonlinearity of asymmetric
al electrode MIIM devices. The good reproducibility, stable J–V behavior, and
centage of working devices along with the enhanced properties achieved
nbining insulator bilayers with asymmetric work function electrodes represent
advancement toward the understanding necessary to engineer thin film MIIM
nel devices for commercial microelectronics applications.

nowledgements This work was supported in part by grants from the National Science
ndation (through DMR-0805372 and an REU supplement), the U.S. Army Research
oratory (through W911NF-07-2-0083), and the Oregon Nanoscience and Microtechnologies
tute. The authors thank Matt Chin, Madan Dubey, and Steve Kilpatrick of the U.S. Army
arch Lab for sputtered Pt films and support, Prof. John Wager, Bill Cowell, and John
llone of the Oregon State University School of Electrical Engineering and Computer
nce for the ZrCuAlNi films used in this study, Prof. Douglas Keszler of the Oregon State
ersity Dept. of Chemistry, Wei Wang for assistance with AFM, Chris Tasker for equipment
ort, Dr. P. Eschbach for assistance with TEM imaging, Cheng Tan and Ben Lambert for
tance with data collection, and Dr. David Evans of Sharp Labs of America for evaporated Ir
Pt films.

ferences

limardani N, Cowell III EW, Wager JF, Conley Jr JF, Evans DR, Chin M, Kilpatrick SJ, ubey M. Impact of electrode roughness on metal-insulator-metal tunnel diodes with atomic yer deposited Al_2O_3 tunnel barriers. J Vac Sci Tech. 2012;A 30:01A113-1–01A113-5.

owell III EW, Alimardani N, Knutson CC, Conley Jr JF, Keszler DA, Gibbons BJ, Wager F. Advancing MIM electronics: amorphous metal electrodes. Adv Mater. 2011;23:74–8.

hoi K, Yesilkoy F, Ryu G, Cho SH, Goldsman N, Dagenais M, Peckerar M. A focused symmetric metal–insulator–metal tunneling diode: fabrication, DC characteristics and RF ctification analysis. IEEE Trans Electron Dev. 2011;58(10):3519–28.

areiß M, Hochmeister A, Jegert G, Zschieschang U, Klauk H, Huber R, Grundler D, orod W, Fabel B, Scarpa G, Lugli P. Printed array of thin-dielectric metal-oxide-metal MOM) tunneling diodes. J Appl Phys. 2011;110:044316- 044316–5.

laraghechi P, Foroughi-Abari A, Cadien K, Elezzabi AY. Enhanced rectifying response from etal-insulator-insulator-metal junctions. Appl Phys Lett. 2011. doi:10.1063/1.3671071.

limardani N, Conley JF Jr, Cowell III, EW, Wager JF, Chin M, Kilpatrick SJ, Dubey . Stability and bias stressing of metal/insulator/metal diodes. IEEE IIRW Final Report. 010. doi: 10.1109/IIRW.2010.5706491.

eriasamy P, Berry JJ, Dameron AA, Bergeson JD, Ginley DS, O'Hayre RP, Parilla A. Fabrication and characterization of MIM diodes based on Nb/Nb_2O_5 via a rapid reening technique. Adv Mater. 2011. doi:10.1002/adma.201101115.

'Regan T, Chin M, Tan C, Birdwell A. Modeling, fabrication, and electrical testing of etal-Insulator-Metal diode. 2011. ARL-TN-0464.

rover S, Moddel G. Engineering the current–voltage characteristics of metal–insulator–metal odes using double-insulator tunnel barriers. Solid State Electron. 2012;67:94–9.

10. Maraghechi P, Foroughi-Abari A, Cadien K, Elezzabi AY. Observation of resonant tunneling phenomenon in metal-insulator-insulator-insulator-metal electron tunnel devices. Appl Phys Lett. 2012. doi:10.1063/1.3694024.
11. Alimardani N, Conley JF Jr. Step tunneling enhanced asymmetry in asymmetric electrode metal-insulator-insulator-metal tunnel diodes. Appl Phys Lett. 2013;102:143501 doi: 10.1063/1.4799964.
12. Corkish R, Green MA, Puzzer T. Solar energy collection by antennas. Sol Energ. 2002;73(6):395–401.
13. B Berland. 2003. NREL SR-520-33263 Final Report.
14. Grover S, Moddel G. Applicability of metal/insulator/metal (MIM) diodes to solar rectennas. IEEE J Photovoltaics. 2011;1:78–83.
15. Miskovsky NM, Cutler PH, Mayer A, Weiss BL, Willis B, Sullivan TE, Lerner PB. Nanoscale devices for rectification of high frequency radiation from the infrared through the visible: a new approach. J Nanotechnol. 2012;2012:1–19.
16. Mead CA. Operation of tunnel-emission devices. J Appl Phys. 1961;32(4):646–52.
17. Heiblum M. Tunneling hot electron transfer amplifiers (theta): amplifiers operating up to the infrared. Solid State Electron. 1981;24:343–66.
18. Sze SM, Ng KK. Physics of semiconductor devices. 3rd ed. Hoboken, NJ: Wiley; 2002.
19. Hobbs PCD, Laibowitz RB, Libsch FR. Ni-NiO-Ni tunnel junctions for terahertz and infrared detection. Appl Optics. 2005;44(32):6813–22.
20. Hobbs PCD, Laibowitz RB, Libsch FR, LaBianca NC, Chiniwalla PP. Efficient waveguide-integrated tunnel junction detectors at 1.6 μm. Opt Express. 2007;15(25):16367–89.
21. Krishnan S, La Rosa H, Stefanakos E, Bhansali S, Buckle K. Effects of dielectric thickness and contact area on current–voltage characteristics of thin film metal-insulator-metal diodes. Thin Solid Films. 2008;516:2244–50.
22. Bean JA, Tiwari B, Bernstein GH, Fay P, Porod W. Thermal infrared detection using dipole antenna-coupled metal-oxide-metal diodes. J Vac Sci Technol B. 2009;27:11–4.
23. Bean JA, Weeks A, Boreman GD. Performance optimization of antenna-coupled Al/AlOx/Pt tunnel diode infrared detectors. IEEE J Quantum Electron. 2011;47(1):126.
24. Bareiß M, Tiwari BN, Hochmeister A, Jegert G, Zschieschang U, Klauk H, Fabel B, Scarpa G, Koblmuller G, Bernstein GH, Porod W, Lugli P. Nano antenna array for terahertz detection. IEEE Trans Micro Technol. 2011;59(10):2751–7.
25. Reuss RH, et al. Macroelectronics: perspectives on technology and applications. Proc IEEE. 2005;93(7):1239–56.
26. den Boer W. Active matrix liquid crystal displays. Amsterdam: Elsevier; 2005.
27. Handy RM. Electrode effects on aluminum oxide tunnel junctions. Phys Rev. 1962;126(6):1968–73.
28. Meyerhofer D, Ochs SA. Current flow in very thin films of Al_2O_3 and BeO. J Appl Phys. 1963;34(9):2535–43.
29. Duke CB. Tunneling in solids. New York: Academic; 1969.
30. Elchinger GM, Sanchez A, Davis Jr CF, Javan A. Mechanism of detection of radiation in a high-speed metal-metal oxide-metal junction in the visible region and at longer wavelengths. J Appl Phys. 1976;47(2):591–4.
31. Heiblum M, Wang S, Whinnery JR, Gustafson TK. Characteristics of integrated MOM junctions at dc and at optical frequencies. IEEE J Quantum Electron. 1978;QE-14(3):159–69.
32. Kleinsasser AW, Buhrman RA. High-quality submicron niobium tunnel junctions with reactive-ion-beam oxidation. J Appl Phys. 1980;37:841–3.
33. Brunner M, Ekrut H, Hahn A. Metal-oxide-metal tunneling junctions on Ta and Nb: background conductivity resulting from different oxide barriers. J Appl Phys. 1982;53(3):1596–601.
34. Grossman EN, Harvey TE, Reintsema CD. Controlled barrier modification in Nb/NbOx/Ag metal insulator metal tunnel diodes. J Appl Phys. 2002;91(12):10134–9.

5. Fisher JC, Giaever I. Tunneling through thin insulating layers. J Appl Phys. 1961;32:172–7.
6. Simmons JG. Conduction in thin dielectric films. J Phys D: Appl Phys. 1971;4:613–57.
7. Simmons JG. Generalized formula for the electric tunnel effect between similar electrodes separated by a thin insulating film. J Appl Phys. 1963;34(6):1793–803.
8. Simmons JG. Electric tunnel effect between dissimilar electrodes separated by a thin insulating film. J Appl Phys. 1963;34(9):2581–90.
9. Miller CW, Li Z, Åkerman J, Schuller IK. Impact of interfacial roughness on tunneling conductance and extracted barrier parameters. Appl Phys Lett. 2007;90:043513.
0. Ekurt H, Hahn A. Polarity-dependent tunneling conductance of $Ta/Ta_2O_5/Ag$ junctions. J Appl Phys. 1980;51:1686–91.
1. Kroemer H. Band offsets and chemical bonding: the basic for heterostructure applications. Physica Scripta. 1996;T68:10–6.
2. Schulz PA, Gonçalves da Silva CET. Two-step barrier diodes. Appl Phys Lett. 1988;52 (12):960.
3. Di Ventra M, Papa G, Coluzza C, Baldereschi A, Schulz PA. Indented barrier resonant tunneling rectifiers. J Appl Phys. 1996;80(7):4174–6.
4. Southwick III RG, Sup A, Jain A, Knowlton WB. An interactive simulation tool for complex multilayer dielectric devices. IEEE Trans Dev Mater Reliab. 2011;11(2):236–43.
5. Inoue A. Stabilization of metallic supercooled liquid and bulk amorphous alloys. Acta Mater. 2000;48:279–306.
6. Sharma P, Zhang W, Amiya K, Kimura H, Inoue A. Nanoscale patterning of Zr-Al-Cu-Ni metallic glass thin films deposited by magnetron sputtering. J Nanosci Nanotechnol. 2005;5:416–20.
7. Sharma P, Kaushik N, Kimura H, Saotome Y, Inoue A. Nano-fabrication with metallic glass—an exotic material for nano-electromechical systems. Nanotechnology. 2007;18 (035302):1–6.
8. Grubbs ME, Zhang X, Deal M, Nishi Y, Clemens BM. Development and characterization of high temperature stable Ta–W–Si–C amorphous metal gates. Appl Phys Lett. 2010; 97:223505-223505-3.
9. Michaelson HB. The work function of the elements and its periodicity. J Appl Phys. 1977;48:4729–33.
0. Crozier KB, Sundaramurthy A, Kino GS, Quate CF. Optical antennas: resonators for local field enhancement. J Appl Phys. 2003. doi:10.1063/1.1602956.
1. Hao E, Schatz GC. Electromagnetic fields around silver nanoparticles and dimers. J Chem Phys. 2004. doi:10.1063/1.1629280.
2. Hashem EI, Rafat NH, Soliman EA. Theoretical study of metal-insulator-metal tunneling diodes figures of merit. IEEE J Quantum Electron. 2013;49(1):72–9.
3. Mott NF. Conduction in non-crystalline materials. Oxford: Oxford University Press; 1993.
4. Dugdale J. The electrical properties of disordered metals. Cambridge: Cambridge University Press; 2005.

Chapter 7
Nanoscale Rectennas with Sharp Tips for Absorption and Rectification of Optical Radiation

N.M. Miskovsky, P.H. Cutler, P.B. Lerner, A. Mayer, B.G. Willis, D.T. Zimmerman, G.J. Weisel, and T.E. Sullivan

Abstract We present a method for optical rectification that has been demonstrated both theoretically and experimentally and can be used for the development of a practical rectification device for the electromagnetic spectrum including the visible portion. This technique for optical frequency rectification is based, not on conventional material or temperature asymmetry as used in MIM or Schottky diodes, but on a purely geometric property of the antenna tip or other sharp edges that may be incorporated on patch antennas. This "tip" or edge in conjunction with a collector anode providing connection to the external circuit constitutes a tunnel junction. Because such devices act as both the absorber of the incident radiation and the rectifier, they are referred to as "rectennas." Using current nanofabrication techniques and the selective Atomic Layer Deposition (ALD) process, junctions of

---

N.M. Miskovsky (✉) • P.H. Cutler
Department of Physics, 104 Davey Laboratory, The Pennsylvania State University, University Park, PA 16802, USA

Scitech Associates, LLC, 232 Woodland Drive, State College, PA 16803, USA
e-mail: nmm1@psu.edu

P.B. Lerner
Scitech Associates, LLC, 232 Woodland Drive, State College, PA 16803, USA

A. Mayer
Facultés Universitaires Notre-Dame de la Paix, Rue de Bruxelles 61, 5000 Namur, Belgium

B.G. Willis
Chemical, Materials & Biomolecular Engineering Department, University of Connecticut, Storrs, CT 06269, USA

D.T. Zimmerman • G.J. Weisel
Division of Mathematics and Natural Sciences, 101 Elm Bldg., Pennsylvania State University, Altoona College, PA 16601, USA

T.E. Sullivan
Department of Electrical & Computer Engineering, Temple University, Philadelphia, PA 19122, USA

G. Moddel and S. Grover (eds.), *Rectenna Solar Cells*,
DOI 10.1007/978-1-4614-3716-1_7, © Springer Science+Business Media New York 2013